eDIG-CHANGES I: extended Hα emission from the extraplanar diffuse ionized gas (eDIG) around CHANG-ES galaxies

Li-Yuan Lu(芦李源) [1], Jiang-Tao Li(李江涛) [2,3]★† Carlos J. Vargas,[4] Rainer Beck,[5] Joel N. Bregman,[3] Ralf-Jürgen Dettmar,[6] Jayanne English,[7] Taotao Fang(方陶陶),[1] George H. Heald [8] Hui Li [9], Zhijie Qu [10] Richard J. Rand,[11] Michael Stein [6] Q. Daniel Wang [12] Jing Wang(王菁),[13] Theresa Wiegert[14] and Yun Zheng[13,15]

Affiliations are listed at the end of the paper

ABSTRACT

The extraplanar diffuse ionized gas (eDIG) represents the cool/warm ionized gas reservoir around galaxies. We present spatial analysis of the Hα images of 22 nearby edge-on spiral galaxies taken with the Apache Point Observatory 3.5-m telescope (eDIG-CHANGES). We conduct an exponential fit to the vertical Hα intensity profiles of the galaxies, of which 16 can be decomposed into thin + thick disk components. The median value of the Hα scale height of the thick disk is $\langle h_{H\alpha} \rangle = 1.13 \pm 0.14$ kpc. We further examine the dependence of $h_{H\alpha}$ on the stellar mass, SFR, and SFR surface density (SFR_{SD}) of the galaxies. We find a tight sublinear correlation between $h_{H\alpha}$ and SFR, expressed in $h_{H\alpha} \propto \text{SFR}^\alpha$, where $\alpha \approx 0.29$. Moreover, the offset of individual galaxies from the best-fit SFR-$h_{H\alpha}$ relation, expressed in $h_{H\alpha}/\text{SFR}^\alpha$, shows significant anti-correlation with SFR_{SD}. We further compare the vertical extension of the eDIG to multi-wavelength measurements of other CGM phases. We find the eDIG slightly more extended than the neutral gas. This indicates the existence of some extended ionizing sources, in addition to the leaking photons from the disk star formation regions. Most galaxies have an X-ray scale height smaller than Hα, suggesting the majority of the X-ray photons are actually from the thick disk instead of the extended CGM. $h_{H\alpha}$ is comparable to the L-band radio continuum scale height. This indicates that the thermal and non-thermal electrons have similar spatial distributions, a natural result if both are transported outwards by a galactic wind. This further indicates the thermal gas, cosmic rays, and magnetic field may be close to energy equipartition.

Key words: galaxies: haloes – galaxies: ISM – galaxies: spiral – galaxies: star formation – galaxies: statistics.

1 INTRODUCTION

The extraplanar diffuse ionized gas (eDIG) plays a key role in the recycling of gas between the galactic disk and halo (Rand 1996; Rossa & Dettmar 2000; Haffner et al. 2009; Putman, Peek & Joung 2012; Levy et al. 2019). The eDIG has been observed in the Milky Way (known as Reynolds layer, e.g. Reynolds 1984) and many other late-type galaxies (e.g. Dettmar 1990; Rand, Kulkarni & Hester 1990; Hoopes, Walterbos & Greenwalt 1996; Hoopes, Walterbos & Rand 1999; Collins & Rand 2001). This gas component typically has a characteristic electron density of $\sim 0.1\,\text{cm}^{-3}$, a temperature of 8000–10 000 K, and radiates strong emission in optical emission lines such as Hα (Reynolds 1985; Haffner, Reynolds & Tufte 1999).

The eDIG could be ionized via various mechanisms. First, it could be photo-ionized by OB stars from star formation regions embedded in the galactic disk (e.g. Reynolds 1984; Zurita et al. 2002; Wood & Mathis 2004; Haffner et al. 2009; Barnes et al. 2015) or an extended Hot Low-mass Evolved Stars component (e.g. Flores-Fajardo et al.

2011). Second, it could be shock ionized by disk outflows, with additional turbulent mixing with the preexisting cold gas envelope or the entrained cold gas clouds (e.g. Chevalier & Clegg 1985; Slavin, Shull & Begelman 1993; Binette et al. 2009). Third, the diffuse Hα emission we observe today may also originate from the gas that was photo-ionized in the past but is currently cooling and recombining (e.g. Dong & Draine 2011). Fourth, the observed extended Hα emission around the disk may also be partialy contributed to by the dust-scattered light of the escaping photons from disk regions with star formation (e.g. Ferrara et al. 1996; Wood & Reynolds 1999; Dong & Draine 2011).

The eDIG is ubiquitous in actively star forming (SF) galaxies (Lehnert & Heckman 1995; Rossa & Dettmar 2000). In most cases, the vertical extension of the global diffuse Hα emission of the eDIG, characterized by the exponential scale height, is typically only ~ 1–2 kpc (Rossa & Dettmar 2003; Jo et al. 2018; Levy et al. 2019). In some galaxies, the eDIG has been detected even up to ~ 5 kpc from the galactic plane (e.g. NGC 891; Rand 1997), and some large scale (mostly filamentary) emission line structures extend up to a few tens of kpc above the disk (e.g. Hodges-Kluck et al. 2020). Morphologically, eDIG around disk galaxies could be classified into at least three components: (1) a diffuse ionized gas envelope

surrounding the galaxy, with a typical vertical extension of a few kpc; (2) some ∼ kpc-scale fine structures at the disk-halo interface such as filaments or bubbles; and (3) some large-scale (typically >10 kpc) filamentary structures connecting the galaxy to the environment.

There are various methods for studying the eDIG around nearby galaxies, including, but not limited to, narrow-band imaging covering some prominent emission lines (e.g. Rossa & Dettmar 2000, 2003), long-slit spectroscopy (e.g. Collins & Rand 2001; Rand 1997; Boettcher, Gallagher & Zweibel 2019), integral field unit (e.g. Boettcher et al. 2016), imaging Fabry-Perot spectroscopy observations (e.g. Heald et al. 2006), etc. Our group is conducting a systematic study of the eDIG around the CHANG-ES galaxies (the eDIG-CHANGES project; this will be introduced in Section 2.1). While our multi-slit spectroscopy observations will be presented in future papers, here we focus on the initial Apache Point Observatory (APO) 3.5-m Hα imaging observations of the sample galaxies (original data obtained from Vargas et al. 2019). We estimate the scale height of the vertical Hα intensity profiles of 22 nearby edge-on galaxies and examine the dependence of this vertical extension on various galactic parameters. We introduce the data analysis in Section 2, then compare our Hα measurements to multi-wavelength galaxy properties and other samples, and discuss the results in Section 3. The major conclusions are summarized in Section 4. Throughout the paper, we quote the errors at 1σ confidence level.

2 SPATIAL ANALYSIS OF THE Hα IMAGES

2.1 Sample

Our sample is comprised of 22 galaxies selected from a comprehensive radio continuum and multi-wavelength survey of 35 nearby edge-on spiral galaxies (CHANG-ES: *Continuum Halos in Nearby Galaxies - an EVLA Survey*; Irwin et al. 2012a, b; Wiegert et al. 2015). The Hα narrow-band images of 25 CHANG-ES galaxies were taken with the APO 3.5m Telescope and the Astrophysical Research Consortium Telescope Imaging Camera, with detailed descriptions of the observation and data reduction procedure presented in Vargas et al. (2019). In the present paper, our aim is to characterize the vertical extension of the eDIG, so we have excluded three galaxies with obviously distorted disks in their Hα images (NGC 660, NGC 2992, NGC 4438). The vignetting correction and/or background subtraction of these Hα images still have some uncertainties, which may affect quantitative measurements of the flux of large-scale features. Therefore, we adopt the Hα images from Vargas et al. (2019) without a flux calibration, in order to avoid any misleading results on flux measurements of large-scale features. The spatial analysis presented in this paper will not be affected, however. The surface brightness sensitivity of these Hα images is in the range of $2.06 - 74.2 \times 10^{-18}$ erg s^{-1} cm^{-2} arcsec^{-2}, with a median value of 8.81×10^{-18} erg s^{-1} cm^{-2} arcsec^{-2}.

We take the redshift independent distance (d), the optical diameter (D_{25}), and the inclination angle (i) from Irwin et al. (2012a); the stellar mass (M_*) and rotation velocity (v_{rot}) from Li et al. (2016); the revised SFR (SFR$_{H\alpha+22\,\mu m}$, based on a combination of the Hα and WISE 22 μm fluxes) and SFR surface density (SFR$_{SD}$) from Vargas et al. (2019). The values of M_* and SFR$_{H\alpha+22\,\mu m}$ are calculated based on a scaled-down Salpeter initial mass function (IMF) (Bell & de Jong 2001) and a Kroupa IMF (Murphy et al. 2011), respectively. All of the galaxies in our sample have high inclination angles ($i \geq 75°$). The key parameters of the sample galaxies are summarized in Table 1.

2.2 Extraction and calibration of the Hα vertical intensity profile

We adopt the continuum-subtracted Hα images from Vargas et al. (2019) to extract the Hα vertical intensity profile. The first step is to detect and mask the optical bright point sources above the disk. We use the sep package (Barbary 2016) and the python module of Source Extractor (Bertin & Arnouts 1996) to detect point sources in the broad-band images taken with a Sloan Digital Sky Survey *r*-band filter. These *r*-band images are also adopted as the continuum filter images in Vargas et al. (2019) We then mask the positions of the detected sources on the Hα images, which could be either foreground or background sources (stars or active galactic nucleus (AGN)), or local sources such as bright compact H II regions. In order to avoid over-masking the fine structures of the disk, we define an elliptical region covering the galactic disk within which we adopt a different source masking criterion. The major axis of the elliptical region is $1.2D_{25}$, while the minor axis is calculated in the same way as in Irwin et al. (2012a),

$$i = 3\deg + \cos^{-1}\left(\sqrt{\left((b/a)^2 - 0.2^2\right)/\left(1 - 0.2^2\right)}\right), \quad (1)$$

where b/a is the minor to major axis ratio. Outside this elliptical region, we mask all the detected point sources, while inside it, we only mask the sources with a diameter less than 10 pixels (pixel size 0.228″). This strategy retains some extended Hα structures, such as H II regions, in the follow-up analysis. The masking process is conducted using the IRAF tool imedit (Tody 1986). We then fill in the masked holes using a linear interpolation of the surrounding pixels. We also manually mask some strong sources that are not appropriately detected, such as some bright H II regions and the luminous nucleus in NGC 4013.

The above procedure generally cleanly removes the contribution from bright compact sources. However, the residual of the reflected or scattered light from bright compact sources may still affect the analysis of the low surface brightness extended emissions, especially when narrow-band filters are used (Karabal et al. 2017; Boselli et al. 2018). We slightly modified the fitting models when some significant reflected or scattered feature is present. For example, such an effect may cause the significantly elevated background level on one side of NGC 5297 (see the online only figures in the Appendix). We therefore only fit the Hα profile of this galaxy with a single component exponential model, which may cause some biases. This galaxy is separated from our main sample in the statistical analysis. We present Hα images and vertical intensity profiles in the Appendix, so readers could appreciate whether individual cases such features could potentially affect the results or not.

Before extracting the vertical profile, a world coordinate system is assigned using IRAF. We combine the Hα images of the galaxies with more than one observation field using Montage (Berriman et al. 2003). We then rotate the Hα images by the position angles of the galaxies. We extract the Hα vertical intensity profile of each galaxy along its minor axis. The horizontal range used to calculate the average value of the intensity is $D_{25}/2$, centered at the mid-plane across the galactic center. As an example, we present the Hα vertical intensity profile and the area used to extract it for the case of NGC 3003 in Fig. 1.

The flat fielding of the Hα images using the twilight flat seems imperfect (Vargas et al. 2019), with a significant residual vignetting effect. Therefore, we fit the background beside the galactic thick

Table 1. Galaxy sample.

Name	d^a Mpc	D_{25}^b arcmin	M_*^c $\times 10^{10}$ M$_\odot$	SFR$_{H\alpha+22\,\mu m}^d$ M$_\odot$ yr^{-1}	SFR$_{SD}^d$ $\times 10^{-3}$ M$_\odot$ yr^{-1} kpc^{-2}	v_{rot}^e km s^{-1}	i^f deg	PA^g deg	scale^h kpc arcsec^{-1}
NGC 2613	23.4	7.2	11.96 ± 0.19	3.36 ± 0.35	3.77 ± 0.39	290.6	85	113	0.11
NGC 2683	6.27	9.1	1.49 ± 0.02	0.25 ± 0.03	3.54 ± 0.40	202.6	79	41.5	0.03
NGC 2820	26.5	4.1	0.467 ± 0.013	1.35 ± 0.14	9.00 ± 0.96	162.8	90	65	0.13
NGC 3003	25.4	6	0.485 ± 0.010	1.56 ± 0.16	2.59 ± 0.27	120.6	90	79	0.12
NGC 3044	20.3	4.4	0.660 ± 0.013	1.75 ± 0.16	6.79 ± 0.60	152.6	90	114	0.10
NGC 3079*	20.6	7.7	4.73 ± 0.07	5.08 ± 0.45	9.57 ± 0.84	208.4	88	75	0.10
NGC 3432*	9.42	4.9	0.100 ± 0.002	0.51 ± 0.06	6.36 ± 0.69	109.9	82	30	0.05
NGC 3448	24.5	4.9	0.564 ± 0.011	1.78 ± 0.18	14.5 ± 1.5	119.5	78	65	0.12
NGC 3556*	14.09	7.8	2.81 ± 0.04	3.57 ± 0.30	7.32 ± 0.62	153.2	81	82.5	0.07
NGC 3628	8.5	14.8	2.83 ± 0.04	1.41 ± 0.12	2.99 ± 0.26	215.4	87	104	0.04
NGC 3735	42.0	4	14.92 ± 0.21	6.23 ± 0.57	6.71 ± 0.61	241.1	85	130	0.20
NGC 3877	17.7	5.1	2.74 ± 0.04	1.35 ± 0.12	5.04 ± 0.44	155.1	85	35	0.09
NGC 4013	16.0	4.7	3.23 ± 0.05	0.71 ± 0.07	3.51 ± 0.32	181.4	84	114	0.08
NGC 4096*	10.32	6.4	0.613 ± 0.010	0.71 ± 0.08	6.52 ± 0.77	144.8	82	17.5	0.05
NGC 4157	15.6	7	2.92 ± 0.04	1.76 ± 0.18	8.15 ± 0.83	188.9	90	63.5	0.08
NGC 4192*	13.55	8.7	3.40 ± 0.05	0.78 ± 0.07	1.67 ± 0.15	214.8	83	150	0.07
NGC 4388	16.6	5.6	1.54 ± 0.02	2.42 ± 0.23	25.0 ± 2.3	171.2	79	89.5	0.08
NGC 4666*	27.5	4.2	12.48 ± 0.18	10.5 ± 0.92	12.8 ± 1.1	192.9	76	40	0.13
NGC 4845	16.98	4.8	2.89 ± 0.05	0.62 ± 0.06	7.33 ± 0.68	176.0	81	75	0.08
NGC 5297	40.4	5.3	3.69 ± 0.07	3.00 ± 0.33	5.70 ± 0.62	189.5	89	153	0.20
NGC 5792	31.7	7.2	8.89 ± 0.16	4.41 ± 0.37	10.0 ± 0.8	208.6	81	81.5	0.15
UGC 10288	34.1	4.9	2.03 ± 0.05	0.66 ± 0.07	1.85 ± 0.21	167.1	90	91	0.17

Notes. *For these galaxies, when fitting the Hα intensity profiles, we exclude the galactic disk area containing 90 per cent of the total emission on each side, instead of 70 per cent for other galaxies.

^{a}Redshift independent distance, from Irwin et al. (2012a).

^{b}Observed blue diameter at the 25th mag arcsec^{-2} isophote, from Irwin et al. (2012a).

^{c}Stellar mass calculated based on a scaled-down Salpeter initial mass function, from Li et al. (2016).

^{d}Star formation rate estimated by combining the Hα and 22μm data (SFR$_{H\alpha+22\,\mu m}$) (adopting a Kroupa IMF) and the corresponding SFR surface density (SFR$_{SD}$), from Vargas et al. (2019).

^{e}The maximum gas rotation velocity corrected for inclination, from Li et al. (2016).

^{f}Inclination angle, from Irwin et al. (2012a).

^{g}Position angle, obtained from NASA/IPAC Extragalactic Database. The adopted values of position angles for some galaxies are slightly adjusted, because the Hα disk may not perfectly align with the stellar disk.

^{h}Physical scale of each galaxy, calculated from the adopted distance.

disk with a second-order polynomial model to account for the curvature of the background, using the curve fitting code LM-FIT.[1] This fitting accounts for both the sky background and a further correction of the flat field. We choose different vertical ranges in the fitting for individual galaxies, excluding prominent Hα emitting features mainly from the galactic disk. The results are in general insensitive to the choice of this fitting range. The background fitting results of individual galaxies are presented in the Appendix, with one example shown in Fig. 1. We then subtract the best-fit background and obtain the flattened intrinsic Hα vertical profile of each galaxy. We notice that in some cases the central region of the vertical profile (close to the disk) may have the background slightly over-subtracted due to the curvature of the second-order polynomial model (e.g. Fig. 1b). This may affect the follow-up exponential fit of the Hα intensity profile, especially the compact component describing the emission significantly affected by the galactic thin disk. This is another reason for not including this component in the scientific analysis (Section 2.3). Furthermore, there may also be some additional uncertainties in continuum subtraction in this area, due to the color gradient of the underlying stellar population (e.g. Spector, Finkelman & Brosch 2012). However, as we are mainly interested in the extended eDIG

distributions, we expect a simple mask of the disk area in the Hα vertical intensity profile should be sufficient to minimize this effect.

2.3 Exponential fit to the Hα vertical profile

Based on previous studies of the eDIG (Rand 1996, 1997; Boettcher et al. 2016; Boettcher et al. 2019; Reach et al. 2020), we need multiple components to describe the distribution of the extraplanar Hα emission. In particular, we fit the profiles above and below the galactic disk separately, to account for the asymmetry of the eDIG. We need to mask the disk since it could be highly affected by emission from the H II regions and extinction by the dust lane. Therefore, we block a region typically containing 70 per cent of the total Hα emission on each side of the disk. For some of the galaxies in the sample, which have unusually extended disk emission or absorption features (most of these are less inclined than the other galaxies, as listed in Table 1), we increase this threshold to 90 per cent to ensure that the eDIG component we are interested in will be well characterized by the exponential model(s). In order to clarify the above choices of blocked disk regions (70 or 90 per cent), we plot them both on the images of individual galaxies and on the vertical intensity profiles (Fig. 1; the Appendix). In many cases, the selected fitting area still includes some disk structures such as the spiral arms (e.g. Fig. 1a). These structures could affect the fitting of the Hα

[1] https://lmfit.github.io/lmfit-py/.
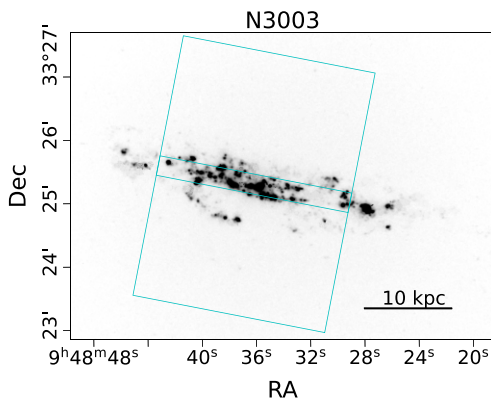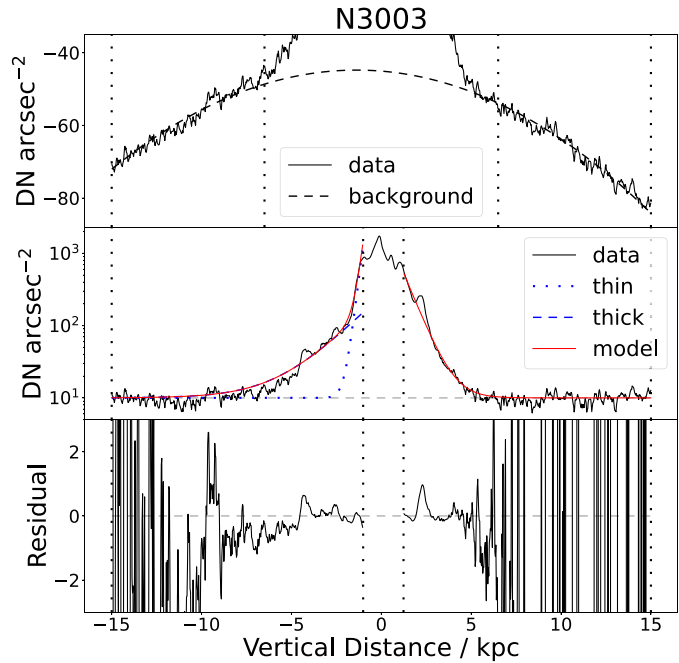
Figure 1. (a) Hα image of NGC 3003 observed with the APO 3.5m telescope. The cyan boxes illustrate the exponential fitting region. The profile is averaged along the major axis. The central region along the disk is excluded from the fitting due to high extinction. (b) Exponential fitting of the vertical Hα intensity profile (with digital number arcsec^{-2} unit) *Top:* background analysis. The solid black curve is the zoomed-in Hα profile to better show the background. The background is fitted with a second-order polynomial model (the dashed black curve). The vertical dotted lines indicate the fitting region boundary. *Middle:* Exponential fit to the background-subtracted Hα intensity profile (black solid curve). The red solid curve is the best-fit exponential model, with the two components (if available) shown as the blue dotted (thin component) and dashed (thick component) curves. The horizontal grey dashed line indicates the zero level with a 10 kpc offset. *Bottom:* residual of the best-fit defined as (*data* − *model*)/*model*.

intensity profiles, especially the compact exponential component. In order to further reduce the influence of the bright compact structures on the analysis of the diffuse extraplanar emission, we perform a Levenberg-Marquardt least-squares fit to minimize the scalar value converted from a negative log-likelihood function in a Cauchy distribution, which is $-\sum \log \left(1/(\pi(1+r^2)) \right)$, where r is the residual array. This method reduces the weight of data points that have a large departure from the fitting model in the fitting process. Those outlier points may be caused by, e.g. spiral arms or off-disk H II regions that were not masked out.

We fit the background-subtracted Hα vertical intensity profiles with a double-exponential function using LMFIT,

$$I_{\mathrm{H}\alpha}(z) = I_{\mathrm{H}\alpha,1}(0)e^{-|z|/h_{z,1}} + I_{\mathrm{H}\alpha,2}(0)e^{-|z|/h_{z,2}}, \qquad (2)$$

where z is the projected distance to the mid-plane of the galaxy, $I_{\mathrm{H}\alpha(,1,2)}(0)$ is the peak intensity of the Hα emission (of each component) at $z = 0$, and $h_{z,1(2)}$ is the scale height of each component. In some cases when the second exponential component is not necessary, we adopt only a single exponential function instead. There is no background component in the function because the background described with a polynomial function has already been subtracted before the fitting. We set $h_{z,2} > h_{z,1}$, so the second component represents the diffuse thick envelope which will be discussed in the following sections, while the first component typically represents the residual of the galactic thin disk. The best-fit values of h_z of each galaxy are listed in Table 2. The subscripts *1* and *2* denote the different components, while *n* and *p* denote different sides of the mid-

plane. As an example, we present the best-fit result of NGC 3003 in Fig. 1(b), where we adopt double and single exponential functions on the two sides, respectively. The figures for other galaxies are presented in the Appendix.

3 RESULTS AND DISCUSSIONS

In our exponential fit of the 22 sample galaxies, 16 have two components at least on one side. The remaining six galaxies can be well fitted with only one exponential component. We notice that the scale heights of these six galaxies (0.41−1.11 kpc) are somewhat comparable to the typical value of the extended component of other galaxies (median value 1.13 ± 0.14 kpc). The lack of the thin disk component may be caused by the strong extinction by the dust lane, which was filtered in the fitting. Alternatively, the extended component of many moderately inclined galaxies may be highly affected by the disk structures, instead of the real extraplanar gas. Regardless, for consistency, we will only include the extended component ($h_{z,2}$) in the following statistical analysis. We will also separate the highly and moderately inclined galaxies in the plots for comparison. For six galaxies where the extended component is detected only on one side (e.g. Fig. 1b), we directly adopt the measured $h_{z,2}$ on this side as the value for this galaxy. The Hα emission on the other side may be largely blocked by the galactic disk, especially when its inclination angle is relatively small. For galaxies with the extended component detected on both sides, we adopt the average value of $h_{z,n,2}$ and $h_{z,p,2}$ in the following analysis. The

Table 2. Exponential fit results of the vertical Hα intensity profiles and corresponding multi-wavelength parameters.

Name	$h_{z,n,1}$ kpc	$h_{z,n,2}$ kpc	$h_{z,p,1}$ kpc	$h_{z,p,2}$ kpc	$h_{H\alpha}$ kpc	h_{HI}^a kpc	h_X^b kpc	h_{Cband}^c kpc	h_{Lband}^c kpc
NGC 2613	1.029 ± 0.129	–	1.107 ± 0.024	–	–	–	–	–	–
NGC 2683	0.232 ± 0.024	0.682 ± 0.089	0.281 ± 0.019	0.714 ± 0.076	0.698 ± 0.059	0.76 ± 0.28	–	–	–
NGC 2820	0.240 ± 0.005	0.837 ± 0.034	0.552 ± 0.030	–	0.837 ± 0.034	–	–	1.16 ± 0.07	1.48 ± 0.19
NGC 3003	0.219 ± 0.033	1.761 ± 0.229	0.713 ± 0.025	–	1.761 ± 0.229	3.48 ± 2.85	–	1.28 ± 0.25	3.66 ± 1.19
NGC 3044	0.249 ± 0.008	1.304 ± 0.148	0.353 ± 0.014	1.224 ± 0.213	1.264 ± 0.130	0.59 ± 0.20	–	1.03 ± 0.11	1.33 ± 0.16
NGC 3079	0.158 ± 0.011	1.062 ± 0.017	0.247 ± 0.024	1.409 ± 0.105	1.235 ± 0.053	1.52 ± 1.02	4.01 ± 0.21	1.54 ± 0.04	1.18 ± 0.19
NGC 3432	0.122 ± 0.002	1.050 ± 0.038	0.168 ± 0.028	0.611 ± 0.084	0.830 ± 0.046	–	–	0.69 ± 0.21	0.93 ± 0.25
NGC 3448	0.291 ± 0.030	1.332 ± 0.289	0.184 ± 0.008	1.011 ± 0.057	1.171 ± 0.147	–	–	–	–
NGC 3556	0.321 ± 0.007	1.404 ± 0.092	0.590 ± 0.009	–	1.404 ± 0.092	1.19 ± 0.35	1.29 ± 0.07	–	–
NGC 3628	0.545 ± 0.002	–	0.603 ± 0.005	–	–	–	3.78 ± 0.69	–	–
NGC 3735	1.046 ± 0.040	–	0.337 ± 0.040	1.710 ± 0.185	1.710 ± 0.185	–	–	1.43 ± 0.23	1.66 ± 0.45
NGC 3877	0.269 ± 0.022	1.284 ± 0.461	0.187 ± 0.003	1.152 ± 0.034	1.218 ± 0.231	1.33 ± 0.22	0.90 ± 0.07	0.86 ± 0.16	1.08 ± 0.17
NGC 4013	0.481 ± 0.033	1.299 ± 0.125	0.315 ± 0.006	1.333 ± 0.037	1.316 ± 0.065	–	1.02 ± 0.15	0.64 ± 0.05	1.03 ± 0.14
NGC 4096	0.216 ± 0.017	0.700 ± 0.163	0.309 ± 0.007	–	0.700 ± 0.163	1.05 ± 0.25	–	–	–
NGC 4157	0.439 ± 0.006	–	0.576 ± 0.009	–	–	0.75 ± 0.28	–	0.99 ± 0.10	1.09 ± 0.07
NGC 4192	0.887 ± 0.047	–	0.826 ± 0.037	–	–	–	–	–	–
NGC 4388	0.134 ± 0.002	0.521 ± 0.006	0.311 ± 0.011	1.171 ± 0.103	0.846 ± 0.052	–	2.00 ± 0.15	–	–
NGC 4666	0.367 ± 0.006	2.609 ± 0.031	0.304 ± 0.005	2.376 ± 0.033	2.492 ± 0.023	–	1.96 ± 0.32	–	–
NGC 4845	0.202 ± 0.026	0.541 ± 0.045	0.251 ± 0.006	0.882 ± 0.024	0.711 ± 0.026	–	–	–	–
NGC 5297	0.411 ± 0.000	–	0.701 ± 0.051	–	–	–	–	–	–
NGC 5792	0.683 ± 0.009	–	0.904 ± 0.107	–	–	–	–	–	–
UGC 10288	0.212 ± 0.037	0.948 ± 0.030	0.346 ± 0.041	1.225 ± 0.053	1.087 ± 0.030	1.17 ± 0.07	–	0.73 ± 0.02	0.84 ± 0.08

Notes. The subscripts 'n' and 'p' denote the negative and positive sides beside the galactic midplane, while '1' and '2' denote the compact and extended components, respectively. $h_{H\alpha}$ is the average value of the negative and positive sides of the extended component, and is used for statistical analysis.
[a] The average scale height of H I 21 cm emission, from Zheng et al. (2022a).
[b] The average scale height of 0.5−1.5 keV emission, from Li & Wang (2013a).
[c] The scale height of the emission in C and L bands, from Krause et al. (2018).

adopted $h_{z,2}$ values of the 16 galaxies calculated this way are in the range of 0.70−2.49 kpc. The median value of $h_{z,2}$ is 1.13 ± 0.14 kpc, consistent with what has been found in previous works (typically ~1–2 kpc; e.g. Rossa & Dettmar 2003).

Using a similar approach adopted in some other CHANG-ES papers (e.g. Li et al. 2016; Vargas et al. 2019), we divide the sample into starburst/non-starburst, and field/clustered subsamples. We define the division of starburst/non-starburst galaxies based on their total SFR and SFR$_{SD}$. A starburst galaxy is defined to have SFR > 1 M$_\odot$ yr^{-1} and SFR$_{SD}$ > 0.002 M$_\odot$ yr^{-1} kpc^{-2}. We define field/clustered galaxies using the local galaxy number density (ρ; Irwin et al. 2012a), which is the density of galaxies brighter than -16 mag in the vicinity of the entry (Tully 1988). Galaxies with $\rho < 0.6$ Mpc^{-3} are classified as being in the field, while those with $\rho > 0.6$ Mpc^{-3} are classified as clustered. In the following analysis, we will plot these different galaxy subsamples with different colors or symbols (starburst: red; non-starburst: black; field: open symbols; clustered: filled symbols; see e.g. Fig. 2). Furthermore, we mark the galaxies that have an identified AGN with a large blue circle (see e.g. Li et al. 2016; Irwin et al. 2019).

We use the Spearman's rank order coefficient (r_s) to describe the goodness of a correlation (e.g. Li & Wang Q. 2013b). In the statistical analysis, we estimate the errors of the fitted or statistical parameters by applying the same analysis to 1000 bootstrap-with-replacement sampled data within their measurement errors. Both the measurement error and the scatter of the sample are taken into account by simultaneously re-sampling both the distribution of the measured parameter values (assuming Gaussian distribution characterized with the errors) and the sample galaxies in the bootstrapping. The same approach has been adopted and detailed in our previous works (e.g. Li & Wang 2013b; Li et al. 2016).
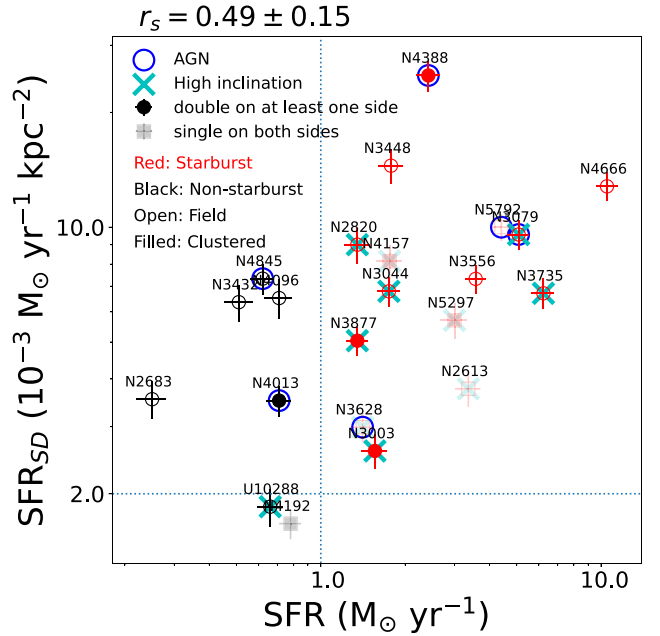

Figure 2. The SFR and the SFR surface density SFR$_{SD}$ of all 22 sample galaxies. Different symbols represent different sub-samples: starburst (red) versus non-starburst (black), field galaxy (open) versus clustered galaxy (filled). The galaxies fitted with just one exponential component on both sides are plotted in square symbols with faded color. Highly inclined galaxies ($i \geq 85°$) are marked by green X-shape symbols. The blue circles represent galaxies hosting an identified radio bright AGN. The two blue dotted lines (SFR = 1 M$_\odot$ yr^{-1} and SFR$_{SD}$ = 0.002 M$_\odot$ yr^{-1} kpc^{-2}) roughly separate starburst and non-starburst galaxies. See Li et al. (2016) for details.
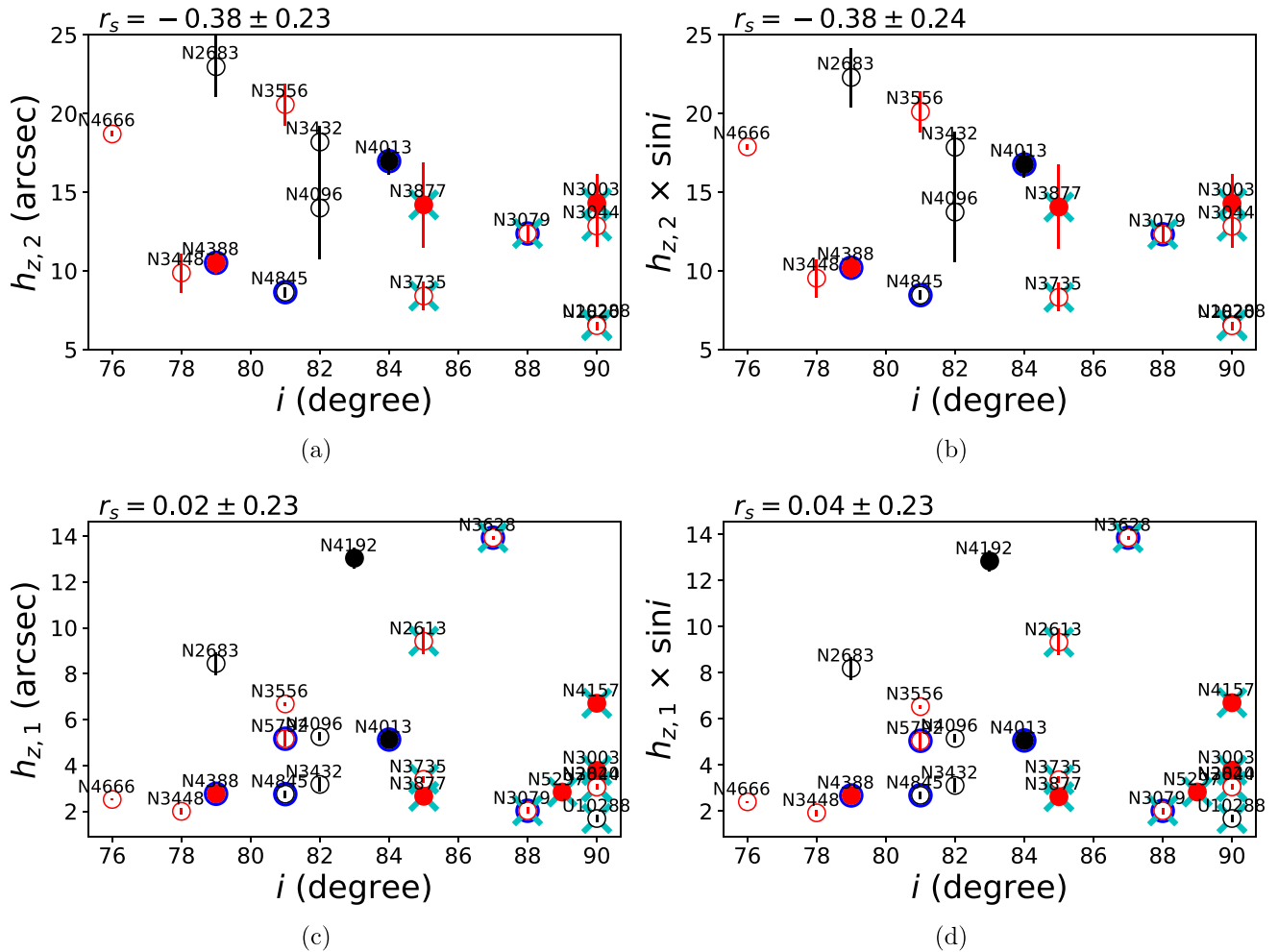
Figure 3. Comparison of the Hα scale heights in (a) component 2 (thick) and (c) component 1 (thin) with the inclination angles (*i*). Panels (b) and (d) show scale heights that have been modified by multiplying with sin *i* in order to check the effect of inclination.

3.1 Contamination caused by the disk inclination

The emission and/or absorption features from the galactic disk may affect our measurement of the Hα scale height, especially in moderately inclined galaxies. We first check the dependence of the measured Hα scale height of the extended component $h_{z,2}$ (with or without a simple geometric correction of the projection) on the inclination angle *i* (Figs 3 a and b). We find no significant correlations between *i* and $h_{z,2}$ ($r_s = -0.38 \pm 0.23$), or $h_{z,2}$ after a simple geometric correction by multiplying by sin *i* ($r_s = -0.38 \pm 0.24$). Because of the lack of correlation between the measured Hα scale height and the inclination angle, and also because our sample galaxies all have high inclination angles ($i = 76° - 90°$), we do not expect a significant systematic bias caused by the extended range of inclination angle of the sample galaxies. Nevertheless, we highlight the highly inclined galaxies ($i \geq 85°$) with a cyan cross in all the plots, in order to examine the potential difference between them and the moderately inclined ones.

Similar results are also shown for the compact component representing the galactic disk (component 1 in equation (2); Section 2.3). Here we find a similar lack of correlation between the Hα scale height and the inclination angle (Figs 3c and d). This component is in principle more significantly affected by some bright highly structured Hα features embedded in or around the disk, such as the

H II regions, filaments, bubbles, etc (e.g. Vargas et al. 2019; Li et al. 2019, 2022). As discussed above, involving this compact component in the statistical analysis could cause confusion in the interpretation of the results. Therefore we focus on the extended eDIG component in the following analysis (the average scale height of the two sides of the extended component is quoted as $h_{H\alpha}$ hereafter; Table 2).

3.2 Dependence of Hα scale height on global galaxy parameters

We plot the measured Hα scale height against various galaxy parameters (SFR, D_{25}, M_*, $v_{rot}^{4.3}$) in Fig. 4. As described in Section 2.1, the SFR is estimated based on a combination of the extinction-corrected Hα emission and the *WISE* 22 μm emission. This revised SFR is systematically higher than the SFR based only on the mid-IR luminosity (Vargas et al. 2019). D_{25} is the observed blue diameter at the 25th mag arcsec^{-2} isophote and is used to represent the size of the galaxies. M_* is the photometric stellar mass estimated using the *Two Micron All-Sky Survey*[2] (*2MASS*) *K*-band magnitude and a color-dependent mass-to-light ratio (Bell & de Jong 2001). v_{rot} is the inclination-corrected rotation velocity obtained from the HyperLeda[3]
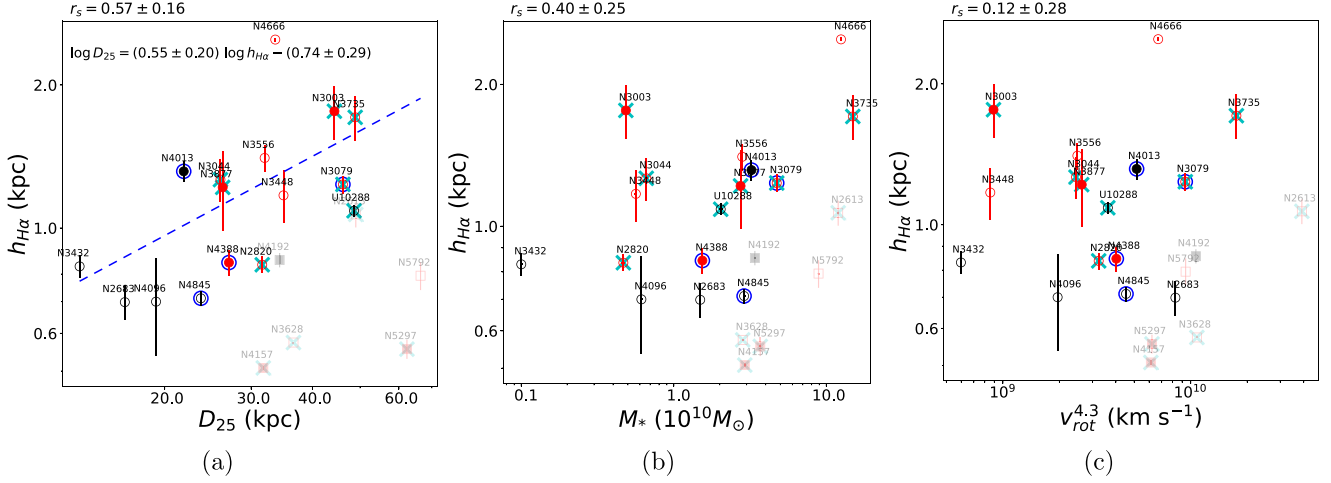
---

[2]https://www.ipac.caltech.edu/project/2mass.
[3]http://leda.univ-lyon1.fr.

Figure 4. The measured scale heights of extended components in Hα emission plotted against the D_{25}, M_*, and $v_{rot}^{4.3}$. Different symbols represent different sub-samples of galaxies as described in Fig. 2. The Spearman's rank order correlation coefficient (r_s) with its 1σ error of each relation is noted at the top left of each panel. The blue dashed line in panel (a) denotes the best-fitting power law model, which is presented at the top of the panel. The galaxies fitted with just one exponential component on both sides (square symbols) are plotted in faded color to facilitate readers.
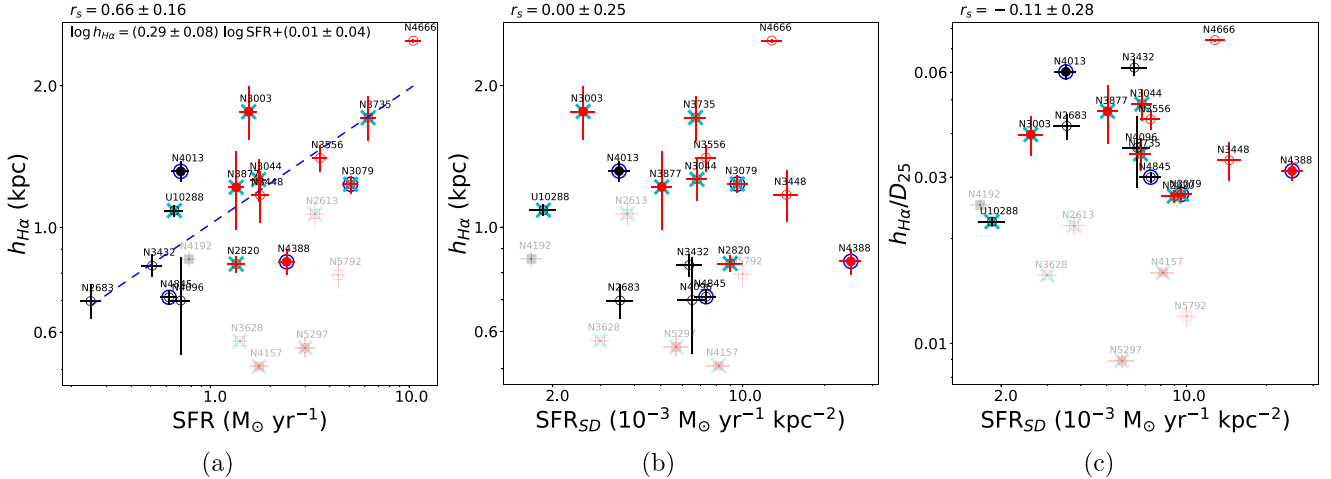

Figure 5. Comparison of the scale heights of the Hα emission with (a) SFR, and (b) SFR_{SD}. (c) Comparison of the normalized scale heights of the Hα emission with SFR_{SD}. The r_s with its 1σ error of each relation is noted at the top left of each panel. The blue dashed line in panel (a) denotes the best-fitting log-log linear line and the relation is presented at the top of the panel.

database. The index 4.3 in $v_{rot}^{4.3}$ is obtained from the baryonic Tully-Fisher relation (Bell & de Jong 2001), so $v_{rot}^{4.3}$ is proportional to the baryonic mass of the galaxy measured in a dynamical way.

We find a tight positive correlation ($r_s = 0.66 \pm 0.16$) between $h_{H\alpha}$ and SFR (Fig. 5a). The best-fit $h_{H\alpha} -$ SFR relation indicates a significant sub-linear slope:

$$h_{H\alpha}/\text{kpc} = 1.02 \pm 0.09 \left(\text{SFR/M}_\odot \text{ yr}^{-1}\right)^{0.29 \pm 0.08}. \quad (3)$$

Many previous works indicate that bright and widespread extraplanar Hα emission is preferentially detected around galaxies with high SFR or high SFR surface density (e.g. Rand 1996; Rossa & Dettmar 2003). However, the connection between the extraplanar Hα features and the disk star formation process may not be the direct reason for the apparent tight $h_{H\alpha}$-SFR correlation, where $h_{H\alpha}$ is mostly determined by the diffuse eDIG component instead of the fine structures. Alternatively, the correlation may be a result of the global scaling relations of the galaxies, which means larger galaxies tend to have both higher global parameters (e.g. mass, SFR, etc.) and larger

extensions of the multi-phase gas (e.g. Wang et al. 2016; Jiang et al. 2019). We will further discuss how to disentangle the global scaling relation from the real physical connection between the eDIG and the SF activity in Section 3.3.

As a result of the global scaling relations, we also find a fairly good correlation between $h_{H\alpha}$ and some other global galaxy parameters such as D_{25} ($r_s = 0.57 \pm 0.16$; Fig. 4a). The slope of the $h_{H\alpha}$-D_{25} relation is sub-linear (0.55 ± 0.20). On the other hand, the correlations between $h_{H\alpha}$ and the mass indicators become significantly poorer ($r_s = 0.40 \pm 0.25$ with M_*; $r_s = 0.12 \pm 0.28$ with $v_{rot}^{4.3}$; Figs 4b and c). Zheng et al. (2022a), Zheng et al. (2022b) found that the scale height of the H I 21 cm emission decreases with the increase of both the total mass surface density and the baryon mass surface density of the galaxies. Such anti-correlations could be explained as a gravitational confinement effect. This effect is also indicated by the sub-linear slope of the $h_{H\alpha} - D_{25}$ relation, which suggests that eDIG of bigger galaxies tends to be more elongated. However, we do not see any significant correlation between $h_{H\alpha}$ and the mass indicators.

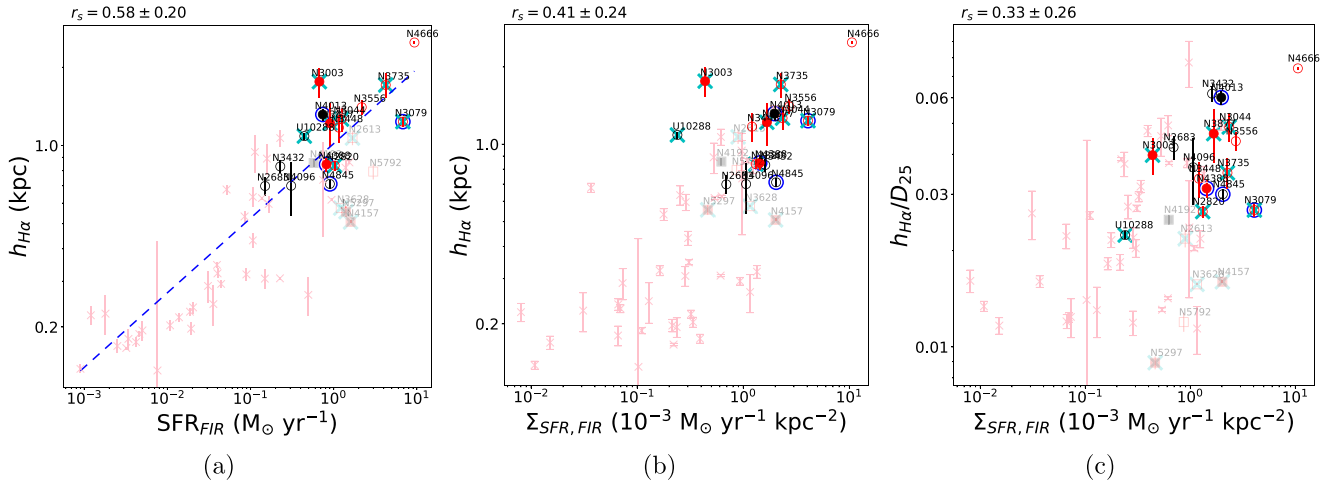**Figure 6.** Comparison of the scale heights of the Hα emission with (a) SFR$_{FIR}$, and (b) $\Sigma_{SFR, FIR}$. (c) Comparison of the normalized scale heights of the Hα emission with $\Sigma_{SFR, FIR}$. The points from Jo et al. 2018 are denoted by pink x-shaped symbols, and these data are not involved in any calculation and fitting in this paper. The measurement and definition of the SFR and SFR surface density are the same for the different samples: SFR$_{FIR}$ is estimated by FIR luminosity and $\Sigma_{SFR,FIR}$ = SFR$_{FIR}/\pi R_{25}^2$, see the context for details. The r_s with its 1σ error of each relation for our sample is noted at the top left of each panel. The blue dashed line in panel (a) is as same as that in Fig. 5(a) and shown here for comparison.

This may be a result of various other effects, such as feedback, which has an opposite effect to the gravitational confinement.

3.3 How does star formation feedback impact the ionized gas distribution?

Star formation and the following feedback of energy and metal-enriched materials are key processes linking the galaxies and their environments. The existence of extraplanar Hα emission around nearby galaxies is believed to be largely related to the active star formation processes in the disk (e.g. Rand 1996; Rossa & Dettmar 2000). However, as discussed in Section 3.2, the apparent correlation between $h_{H\alpha}$ and the global galaxy parameters including the SFR is not necessarily caused by the real connection between the star formation processes and the eDIG.

In a sample of 38 nearby edge-on galaxies, Jo et al. (2018) reported even tighter correlations between $h_{H\alpha}$ and the SFR or the SFR surface density (Σ_{SFR}) than reported in the present paper, which is largely caused by the extension of their sample to lower SFR or Σ_{SFR} (Fig. 6). In addition, they also reported a weak correlation between the normalized Hα scale height ($h_{H\alpha}/D_{25}$) and Σ_{SFR}, which is quite marginal in our sample (Fig. 6c). We caution that the SFR and its surface density are measured in a different way in the present paper than in Jo et al. (2018). Our SFR$_{SD}$ is calculated from the revised SFR (SFR$_{H\alpha+22\,\mu m}$, based on a combination of the Hα and mid-IR data; Vargas et al. 2019) and the mid-IR-based star formation radius (measured from the *WISE* 22 μm image; Wiegert et al. 2015):

$$SFR_{SD} = SFR_{H\alpha+22\,\mu m}/\left(\pi R_{22}^2\right), \qquad (4)$$

where R_{22} is the 22 μm radii from Wiegert et al. (2015). In contrast, Jo et al. (2018) calculated Σ_{SFR} from the far-IR-based SFR and the optical diameter D_{25}:

$$\Sigma_{SFR,FIR} = SFR_{FIR}/\left(\pi D_{25}^2\right). \qquad (5)$$

In the figures presented in this paper, we have replaced the diameter D_{25} with the corresponding radius R_{25} in the above equation and re-calculated $\Sigma_{SFR, FIR}$ for Jo et al.'s (2018) sample. For a more consistent comparison, we also calculate SFR$_{FIR}$ and $\Sigma_{SFR, FIR}$ for

our sample galaxies using the same definition as adopted in Jo et al. (2018). We quote the FIR luminosity L_{FIR} of our sample from Irwin et al. (2012a) and calculate SFR$_{FIR}$ using the relation from Kennicutt (1998). We also caution that although the FIR luminosity in Irwin et al. (2012a) and Jo et al. (2018) are both calculated from the *IRAS* 60 and 100 μm fluxes (f_{60} and f_{100}; using the relation in Sanders & Mirabel 1996), the fluxes are indeed quoted from different references. Jo et al. (2018) quoted the values from Moshir et al. (1990) and Irwin et al. (2012a) quoted them from Sanders et al. (2003), except for several galaxies that used the most recent entry listed in NASA/IPAC Extragalactic Database, usually from the IRAS Faint Source Catalog.

We compare our sample to Jo et al.'s (2018) sample in Fig. 6. Our sample is in general well consistent with that of Jo et al. (2018) on the global $h_{H\alpha} - SFR_{FIR}$ relation, and most of our $\sim L^\star$ galaxies are located in the high SFR range because they are generally more massive (Fig. 6a). The SFR surface density $\Sigma_{SFR, FIR}$ is a normalized entity and for this reason it is a better tracer of the intrinsic activity of star formation in galaxies. In Figs 6(b) and (c), we compare our sample to that of Jo et al. (2018) by plotting $h_{H\alpha}$ and $h_{H\alpha}/D_{25}$ against $\Sigma_{SFR, FIR}$. It is clear that the two samples are consistent with each other on the relations, and show significant positive correlations. This indicates real positive effects of star formation on the vertical extension of the eDIG, as also suggested by many previous works (e.g. Collins et al. 2000; Rossa & Dettmar 2000; Haffner et al. 2009).

We also notice a fairly strong anti-correlation between $h_{H\alpha}/SFR^{0.29}$ and SFR$_{SD}$ ($r_s = -0.54 \pm 0.22$; Fig. 7). Here the index 0.29 is the best-fit power-law index of the $h_{H\alpha} - SFR$ relation (Fig. 5a), the strongest correlation between $h_{H\alpha}$ and the global galaxy parameters. Therefore, $h_{H\alpha}/SFR^{0.29}$ describes the offset of different galaxies from the best-fit $h_{H\alpha} - SFR$ relation, or the residual of the primary correlation which may be affected by the secondary effects. The clear anti-correlation between $h_{H\alpha}/SFR^{0.29}$ and SFR$_{SD}$, together with the sublinear $h_{H\alpha} - SFR$ relation, suggests that the size of the eDIG is disproportionately scaled to the star formation activity, or a more actively SF galaxy will tend to extend the eDIG less efficiently.

The eDIG could be ionized in various ways. The most common one is by photo-ionization caused by leaking Lyman continuum (LyC)
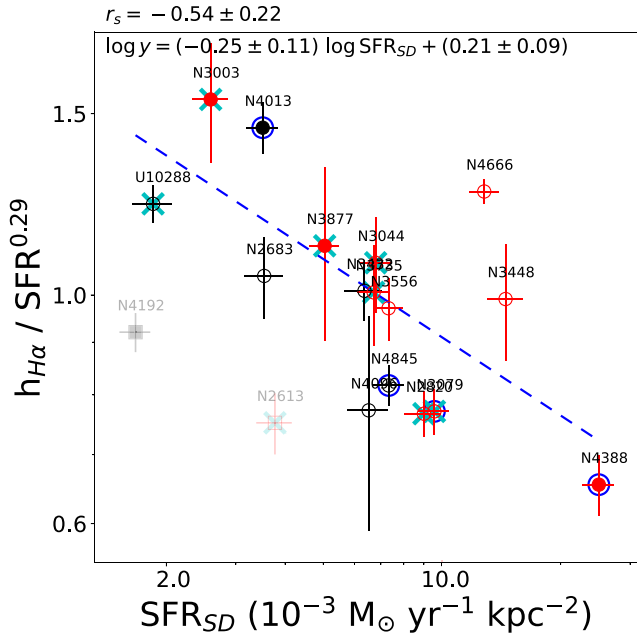
$r_s = -0.54 \pm 0.22$

$\log y = (-0.25 \pm 0.11) \log \mathrm{SFR}_{SD} + (0.21 \pm 0.09)$

Figure 7. The offsets in the $h_{\mathrm{H}\alpha} - $ SFR relation plotted against the SFR surface density (SFR$_{SD}$). The r_s with its 1σ error is noted at the top left. The blue dashed line denotes the best-fitting log-log linear lines and the relation is presented at the top right.

photons from H II regions embedded in the galactic disk (e.g. Rozas, Beckman & Knapen 1996; Zurita, Rozas & Beckman 2000; Tacchella et al. 2022). Some other processes may also contribute, including, but not limited to, shock-ionization (e.g. Chevalier & Clegg 1985), turbulence (e.g. Slavin et al. 1993; Binette et al. 2009), in situ ionization by decaying massive neutrinos (e.g. Sciama 1990), and/or extra ionizing photons from the UV background (e.g. Madau & Haardt 2015). In case of photo-ionization, the vertical distribution of the Hα emission is determined mainly by two factors: the vertical distribution of the neutral gas and the vertical distribution of the ionizing photons. The disk star formation activity could strongly affect the intensity of the ionizing photons, but have less effect on the global distribution of the neutral gas reservoir.

When the eDIG is mostly ionized by some external sources such as the uniform UV background, its extension is mostly affected by the distribution of the gas instead of the ionizing photons, so we do not expect a tight correlation between $h_{\mathrm{H}\alpha}$ and the SFR surface density. But a positive $h_{\mathrm{H}\alpha}$-SFR correlation is still expected as bigger galaxies tend to have both larger SFR and more extended gas reservoirs. On the other hand, if internal ionizing sources, such as LyC photons or shock, dominate the ionization of the eDIG, $h_{\mathrm{H}\alpha}$ will be highly affected by the star formation activity. The former case (external ionizing source dominates) appears at large vertical distances from the disk or in quiescent galaxies, while the latter case (internal ionizing source dominates) appears close to an actively SF disk. The vertical Hα scale height is a characterization of the overall distribution of the eDIG, which is not only affected by its outermost extension. When the SFR surface density increases, not only the outermost extension of the eDIG increases, but also the Hα emission tends to be more concentrated toward the galactic plane due to its high photon intensity and gas density. The latter effect could even reduce the vertical scale height. The combined effect is just a slight increase of $h_{\mathrm{H}\alpha}$, as indicated by the significant sublinear $h_{\mathrm{H}\alpha}$-SFR relation (Figs 5 a and 6a). Furthermore, the possible negative effect of

intense star formation on $h_{\mathrm{H}\alpha}$ is also indicated by the anti-correlation between $h_{\mathrm{H}\alpha}/\mathrm{SFR}^{0.29}$ and SFR$_{SD}$ (Fig. 7), which means galaxies with a high SFR$_{SD}$ disproportionately increase $h_{\mathrm{H}\alpha}$ compared to less active galaxies. Li & Wang (2013b) discovered a similar effect in their X-ray studies of a sample of edge-on galaxies, where the X-ray radiation efficiency, or the offset of the first order $L_X - \dot{E}_{SN}$ relation (L_X is the X-ray luminosity of the galactic halo, while $\dot{E}_{SN}$ is the total SN energy injection rate), also shows an anti-correlation with the SN rate surface density (roughly proportional to the SFR surface density in late-type galaxies). The observed relations between the eDIG extension and the star formation properties are caused by a combination of many complicated processes, and so appear to have a large scatter. Detailed theoretical modeling, in comparison with deeper optical emission line observations, are needed to unveil the impact of star formation feedback on the eDIG (e.g. Tacchella et al. 2022).

3.4 Vertical extension of different CGM phases

In this section, we compare our Hα scale height of the eDIG to the vertical scale heights of a few other circum-galactic medium (CGM) phases obtained from multi-wavelength observations of the CHANG-ES galaxies: the H I 21 cm line tracing the neutral hydrogen (h_{HI}; Zheng et al. 2022a, b), the soft X-ray emission tracing the hot gas (h_X; Li & Wang 2013a), and the radio continuum emission at C-band (centered at 6 GHz) and L-band (centered at 1.5 GHz) tracing the synchrotron emission of cosmic ray (CR) electrons in the galactic scale magnetic field (h_C and h_L; Krause et al. 2018). The results are presented in Fig. 8, where the black dot-dashed line in each panel indicates where the scale heights of the two phases included in the comparison are equal to each other. We caution that due to the limited number of objects with reliable multi-wavelength measurements, the large uncertainty in the measured scale heights, and the low statistical significance of the relations (see below), the comparisons in this section are largely initial and far from conclusive. But they still show some potentially interesting trends which may worth discussions and some further observational confirmations in the future.

We first compare our Hα scale height to the H I 21 cm line scale height obtained from Zheng et al. (2022a), Zheng et al. (2022b) (Fig. 8a). Zheng et al. (2022a), Zheng et al. (2022b) studied the H I 21 cm line emission from 19 galaxies based on CHANG-ES L-band data observed with the *VLA* in its C-configuration. These wide-band observations were designed to detect the radio continuum halo, so they are not optimized for studying narrow emission lines, especially their dynamics. Nevertheless, Zheng et al. (2022a), Zheng et al. (2022b) could still extract the H I 21 cm line vertical profile and measure its global scale height.

Only eight galaxies have reliable measurements of the scale heights in both our Hα sample and Zheng et al. (2022a), Zheng et al. (2022b)'s H I sample. Most of the galaxies have $h_{\mathrm{H}\alpha} < h_{\mathrm{HI}}$ (Fig. 8a). The median value of $h_{\mathrm{H}\alpha}/h_{\mathrm{HI}}$ is 0.7 ± 0.1. A smaller $h_{\mathrm{H}\alpha}$ than h_{HI} has also been revealed in some previous works on nearby edge-on galaxies, often indicating an extended H I envelope (e.g. Reach et al. 2020). Since the Hα emission is $\propto n_e^2$, while the H I emission is $\propto n_{\mathrm{HI}}$, we also plot a line of $h_{\mathrm{H}\alpha} = 1/2h_{\mathrm{HI}}$ in Fig. 8(a), which marks where the Hα emission exactly follows the distribution of the atomic gas. Most of the galaxies have $h_{\mathrm{H}\alpha}$ slightly larger than $1/2h_{\mathrm{HI}}$. Therefore, the eDIG may be slightly more vertically extended than the atomic CGM. This could possibly be consistent with the existence of some extended sources of ionizing photons, either from the UV background or from the escaped LyC
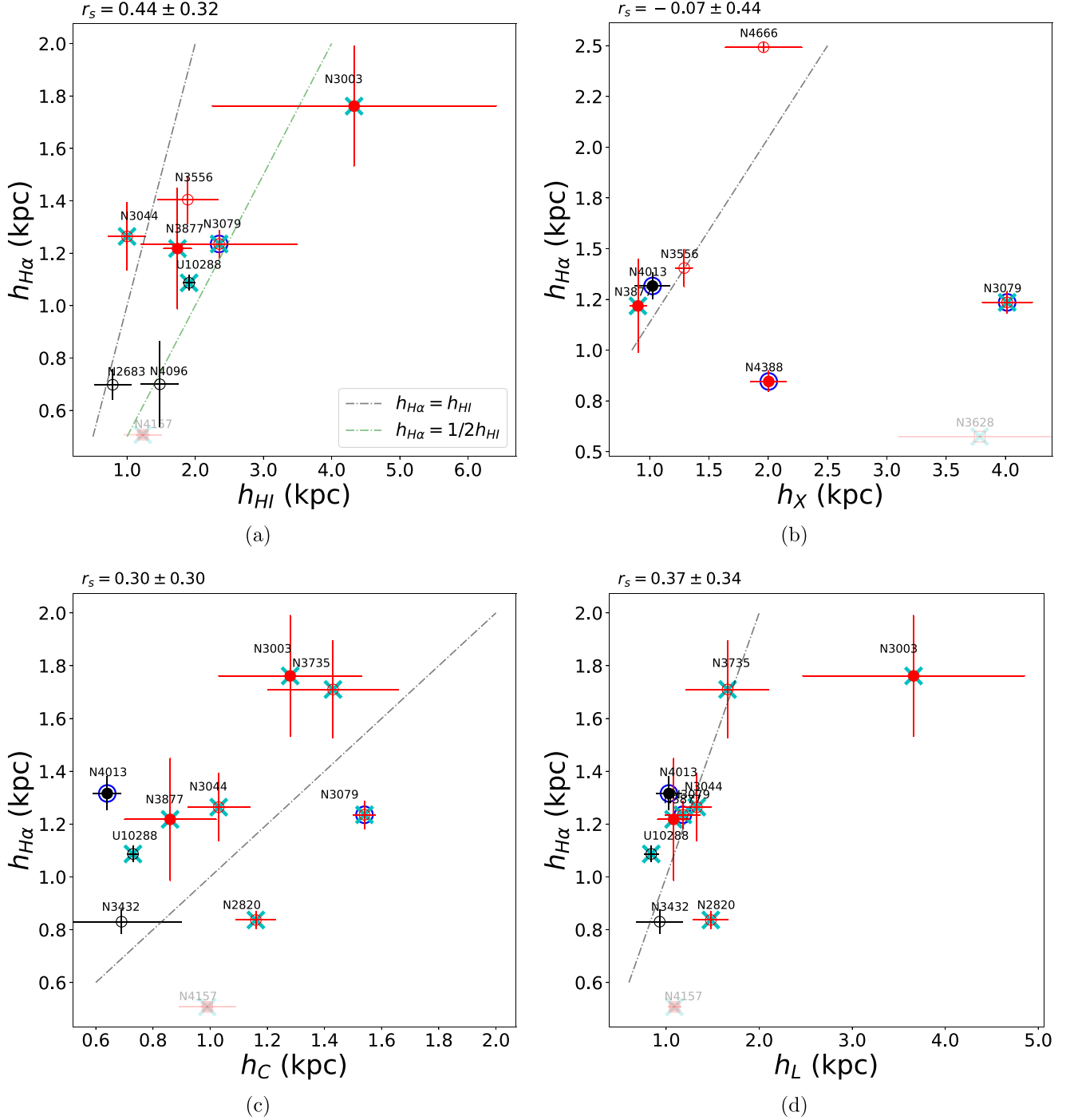
Figure 8. Comparison of the scale heights of the Hα emission with those of (a) H I 21 cm, (b) X-ray, (c) radio C-band, and (d) L-band emission. The black dot-dashed lines indicate one-to-one correspondence lines. The green dot-dashed line in panel (a) indicates the line where $h_{H\alpha} = 1/2 h_{HI}$. The value of r_s with its 1σ error of each relation is noted at the top left of each panel.

photons from the galactic disk. We caution that the Hα and H I scale heights adopted in the present paper are both insensitive to the large scale structures (partially caused by the high detection limit of the observations; Zheng et al. 2022a), so the comparison here is probably only sensitive to the compact gas components close to the disk. For example, because the radiative cooling curve peaks at the typical temperature of the warm ionized gas (Sutherland & Dopita 1993), the radiative cooling timescale of the eDIG is often small

compared to that of the hot or cold gases or the dynamical timescale of the galaxies. The warm gas in the eDIG thus tends to cool fast and form some filamentary structures. These structures have been detected in optical emission lines on different scales from sub-kpc to ~10^2 kpc (e.g. Li et al. 2008, 2019, 2022; Kenney et al. 2008; Rupke et al. 2019; Hodges-Kluck et al. 2020). Because of their low filling factors, our vertical intensity profiles are generally insensitive to these fine structures. Therefore, the vertical extension of the eDIG

quoted here only includes the diffuse component and could bias the comparison.

NGC 3044 is the only galaxy in our sample whose Hα scale height is larger than the H I scale height (Fig. 8a). This galaxy has a relatively high dynamical-to-stellar mass ratio ($M_{TF}/M_* \sim 4.12 \pm 0.08$, where M_{TF} is the mass calculated with the rotation velocity v_{rot} and the Tully-Fisher relation, while M_* is the photometric stellar mass, both from Li et al. 2016). This is significantly higher than the average value of all the CHANG-ES galaxies ($M_{TF}/M_* \sim 2.44 \pm 0.01$). The high M_{TF}/M_* value could be a result of the deeper gravitational potential which may help to confine the cold atomic gas close to the mid-plane of the galaxy (Richards et al. 2018). Another galaxy, NGC 3003, shows an unusually large H I scale height, together with a very extended eDIG. The extended and distorted multi-phase CGM could be explained by the tidal interaction with the neighboring galaxy NGC 3021 (Hoopes et al. 1999; Karthick et al. 2004).

X-ray emission from the halos of disk galaxies are most commonly explained as the hot gas produced by stellar feedback (e.g. Li & Wang 2013b; Li, Wang & Crain 2014). The eDIG layer or some fine structures in it are found to be spatially correlated with coherent soft X-ray emission features (e.g. Strickland et al. 2004; Tüllmann et al. 2006a, b; Li et al. 2008, 2019, 2022). Li & Wang (2013a) studied the large-scale diffuse soft X-ray emission around 53 nearby and highly inclined disk galaxies observed by *Chandra*, and measured the exponential scale height of the point-source-removed $0.5 - 1.5$ keV emission. Although there are only six galaxies with reliable measurements in both Hα and X-ray, it seems that most galaxies tend to have an X-ray scale height smaller than the Hα scale height, except for two outliers: NGC 4388 and NGC 3079 (Fig. 8b). These two galaxies are well known for their extremely large Hα and X-ray filaments extending to a few tens of kpc above the disk (e.g. Cecil et al. 2001; Yoshida et al. 2002; Iwasawa et al. 2003; Strickland et al. 2004; Kenney et al. 2008; Li et al. 2019; Hodges-Kluck et al. 2020). However, the Hα filaments always appear much thinner than the coherent X-ray filaments, because they are intrinsically denser and less volume filling, and also because the Hα images typically have higher angular resolutions than the X-ray images. Therefore, these large scale filaments may not contribute significantly in our Hα scale height measurements, but they could largely affect the X-ray scale height. If we do not consider these two outliers, the typically smaller scale height in X-ray than in Hα may suggest that X-ray emission detected with typically shallow exposures is actually from the thick disk in the close vicinity of the galaxies instead of the extended CGM, representing the interplay between hot and cool gases (Bogdán et al. 2013; Anderson, Churazov & Bregman 2016; Li et al. 2017, 2018).

Krause et al. (2018) measured the radio continuum scale heights in C-band (centered at 6 GHz) and L-band (centered at 1.5 GHz) of 13 CHANG-ES galaxies, by applying a two-component exponential function. They found no clear correlations between the radio scale heights and the SFR or SFR surface density. The average values of the radio scale heights of the extended halo component are $h_C = 1.1 \pm 0.3$ kpc in C-band and $h_L = 1.4 \pm 0.7$ kpc in L-band, which are comparable to the median Hα scale height obtained in the present paper (1.13 ± 0.14 kpc). As shown in Figs 8(c) and (d), except for the significantly larger L-band scale height of NGC 3003 (and possibly the slightly larger radio scale heights of NGC 2820 in both bands), most of the galaxies have a smaller scale height in C-band, while a comparable scale height in L-band, than the Hα scale height. The scale height of the C-band emission is smaller than those of the L-band and Hα. This could

be explained by the stronger synchrotron cooling at the higher CR electron energy or a larger fraction of thermal radio emission at higher frequencies (e.g. Vargas et al. 2018). The most significant outlier, NGC 3003, as mentioned above, is a galaxy undergoing interaction with a neighboring galaxy, which may result in unusually large radio features, at least on low resolution images. Furthermore, there exists a background radio source projected close to the disk of this galaxy, which may also bias the radio scale height measurements (Wiegert et al. 2015). This galaxy is also a significant outlier in many statistical analyses of radio scale heights (Krause et al. 2018).

The comparable scale heights in Hα and L-band might not be by chance. The synchrotron emission intensity can be described as:

$$I_{syn} \propto n_{CRE} B^{1+\alpha_{syn}}, \qquad (6)$$

where n_{CRE} is the number density of the CR electrons responsible for the synchrotron emission, B is the magnetic field strength, and α_{syn} is the synchrotron spectral index. Therefore, the corresponding scale heights of the synchrotron emission, CR electrons, and the magnetic field, have the following relationship:

$$1/h_{syn} = 1/h_{CRE} + (1+\alpha_{syn})/h_B. \qquad (7)$$

If we assume energy equipartition between the CR electrons and the magnetic field, i.e. $n_{CRE} \propto B^2$, we can obtain $h_{CRE} = h_B/2$. Substituting this into equation (7), we can obtain the relation between the synchrotron emission scale height and the CR electron or magnetic field scale height:

$$h_{syn} = h_B/(3+\alpha_{syn}),$$
$$h_{syn} = 2h_{CRE}/(3+\alpha_{syn}). \qquad (8)$$

α_{syn} depends on the star formation properties. For most of the CHANG-ES galaxies without a radio-bright AGN, the typical value of α_{syn} is ~ 1 (Li et al. 2016). Therefore, we obtain $h_{syn} = h_B/4 = h_{CRE}/2$. On the other hand, as the Hα emission $I_{H\alpha} \propto n_e^2$ (here n_e is the thermal electron density), we can obtain $h_{H\alpha} = h_e/2$. From Fig. 8(d), we see $h_{H\alpha} \approx h_L$, so $h_e \approx h_{CRE}$.

The thermal and non-thermal electrons are produced by different mechanisms, but they have comparable scale heights. This indicates that they may be linked in some ways. A possible explanation is that both of them are transported outwards by an accelerating galactic wind. They suffer from the same adiabatic expansion, so their vertical distributions are similar. The similar scale heights of the thermal and non-thermal electrons could even indicate energy equipartition between the thermal gas and the CR electrons, as also suggested in magnetohydrodynamics (MHD) simulations at a relatively small distance from the galactic plane (e.g. $z \lesssim 1$ kpc; Girichidis et al. 2018). However, we caution that at larger distances, the CR pressure typically decreases slower than the thermal pressure and could play a more important role (e.g. Everett et al. 2008; Girichidis et al. 2018; Hopkins et al. 2020).

4 SUMMARY

In this paper, we present measurements and a statistical analysis of the eDIG of 22 CHANG-ES galaxies, using on Hα images taken with the APO 3.5-m telescope. We characterize the vertical extension of the Hα emission with a two-component exponential model. While the compact component in the two-component model is thought to be the galactic thin disk, we assume that the extended component represents the extended Hα envelope or the thick disk surrounding the galaxies. The latter is used in the follow-up statistical analysis.

The median Hα scale height of the thick disk component for the 16 galaxies where it is detected is $\langle h_{H\alpha} \rangle = 1.13 \pm 0.14$ kpc. We also compare $h_{H\alpha}$ of our sample galaxies to those from a bigger sample, including dwarf galaxies. We examined the relation between $h_{H\alpha}$ and some global galaxy parameters, and find a tight sub-linear (with a logarithm slope of $\alpha = 0.29$) correlation between $h_{H\alpha}$ and the SFR. We also find an anti-correlation between the offsets from the best-fit SFR-$h_{H\alpha}$ relation (characterized by $h_{H\alpha}/SFR^{\alpha}$, where $\alpha = 0.29$) and the SFR surface density, SFR_{SD}. This secondary effect indicates that galaxies with more intense star formation tend to have disproportionately extended eDIG compared to those with less intense star formation. The vertical extension of the eDIG is affected by both the spatial distribution of neutral gas and ionizing photons, which need to be further studied with numerical simulations and deeper Hα observations.

Based on the multi-wavelength data collected by the CHANG-ES consortium, we further compare the vertical extensions of the eDIG and the other phases of the CGM. When comparing to the H I 21-cm line scale height measured from the CHANG-ES *VLA* data, we find that most of the galaxies have $h_{H\alpha}/h_{HI} = 0.5 - 1$, with a median value of $\langle h_{H\alpha}/h_{HI} \rangle = 0.7 \pm 0.1$. This means that the thick disk component of the eDIG is slightly more extended than the cold neutral gas envelope, not accounting for the very extended component of both phases. Most galaxies have an X-ray scale height smaller than the Hα scale height, suggesting that the majority of the X-ray emission detected in shallow observations is actually from the thick disk rather than the extended CGM.

The Hα scale height is in general comparable to the L-band radio continuum scale height, both slightly larger than the scale height at higher radio frequencies (C-band). This indicates that the thermal and non-thermal electrons have similar spatial distributions, at least close to the galactic disk, a natural result if both of them are transported outwards by a galactic wind. This explanation further indicates that the thermal gas, the CRs, and the magnetic field are probably close to energy equipartition, which has important implications in understanding the galactic outflow. The smaller scale height in C-band could be explained by a stronger synchrotron cooling or a larger thermal fraction at higher frequencies.

APPENDIX

Images and Hα vertical intensity profiles of individual galaxies are included in the appendix as online only supplementary materials. These figures of individual galaxies are similar as the example shown in Fig. 1.

ACKNOWLEDGEMENTS

DATA AVAILABILITY

The Hα images and vertical intensity profiles of individual galaxies are available as supplementary materials. Figures of them will be put online only. The original data could be shared by reasonable request to the corresponding author.

REFERENCES

Anderson M. E., Churazov E., Bregman J. N., 2016, MNRAS, 455, 227
Barbary K., 2016, JOSS, 1, 58
Barnes J. E., Wood K., Hill A. S., Haffner L. M., 2015, MNRAS, 447, 559
Bell E. F., de Jong R. S., 2001, ApJ, 550, 212
Berriman G. B., Good J. C., Curkendall D. W. et al., 2003, in ASP Conf. Ser. Vol. 295. p. 343
Bertin E., Arnouts S., 1996, A&A, 117, 393
Binette L., Flores-Fajardo N., Raga A. C., Drissen L., Morisset C., 2009, ApJ, 695, 552
Boettcher E., Zweibel E. G., Gallagher J. S., III, Benjamin R. A., 2016, ApJ, 832, 118
Boettcher E., Gallagher J. S., III, Zweibel E. G., 2019, ApJ, 885, 160
Bogdán Á. et al., 2013, ApJ, 772, 97
Boselli A. et al., 2018, A&A, 614, A56
Cecil G., Bland-Hawthorn J., Veilleux S., Filippenko A. V., 2001, ApJ, 555, 338
Chevalier R. A., Clegg A. W., 1985, Natur, 317, 44
Collins J. A., Rand R. J., 2001, ApJ, 551, 57
Collins J. A., Rand R. J., Duric N., Walterbos R. A. M., 2000, ApJ, 536, 645
Dettmar R.-J., 1990, A&A, 232, L15
Dong R., Draine B. T., 2011, ApJ, 428, 647
Everett J. E., Zweibel E. G., Benjamin R. A., McCammon D., Rocks L., Gallagher J. S. III, 2008, ApJ, 674, 258
Ferrara A., Bianchi S., Dettmar R.-J., Giovanardi C., 1996, ApJ, 467, L69
Flores-Fajardo N., Morisset C., Stasińska G., Binette L., 2011, MNRAS, 415, 2182
Girichidis P., Naab T., Hanasz M., Walch S., 2018, MNRAS, 479, 3042
Haffner L. M., Reynolds R. J., Tufte S. L., 1999, ApJ, 523, 223
Haffner L. M. et al., 2009, RMP, 81, 969
Heald G. H., Rand R. J., Benjamin R. A., Collins J. A., Bland-Hawthorn J., 2006, ApJ, 636, 181
Hodges-Kluck E., Yukita M., Tanner R., Ptak A. F., Bregman J. N., Li J.-T., 2020, ApJ, 903, 35
Hoopes C. G., Walterbos R. A. M., Greenwalt B. E., 1996, AJ, 112, 1429
Hoopes C. G., Walterbos R. A. M., Rand R. J., 1999, ApJ, 522, 669
Hopkins P. F. et al., 2020, MNRAS, 492, 3465
Irwin J. et al., 2012a, AJ, 144, 43
Irwin J. et al., 2012b, AJ, 144, 44
Irwin J. et al., 2019, AJ, 158, 21
Iwasawa K., Wilson A. S., Fabian A. C., Young A. J., 2003, MNRAS, 345, 369
Jiang X., Li J., Fang T., Wang Q. D., 2019, ApJ, 885, 38
Jo Y.-S., Seon K.-i., Shinn J.-H., Yang Y., Lee D., Min K.-W., 2018, ApJ, 862, 25
Karabal E., Duc P.-A., Kuntschner H., Chanial P., Cuillandre J.-C., Gwyn S., 2017, A&A, 601, A86
Karthick M. C., López-Sánchez Á. R., Sahu D. K., Sanwal B. B., Bisht S., 2014, MNRAS, 439, 157
Kenney J. D. P., Tal T., Crowl H. H., Feldmeier J., Jacoby G. H., 2008, ApJ, 687, 69
Kennicutt R. C. Jr, 1998, ApJ, 498, 541
Krause M. et al., 2018, A&A, 611, A72
Lehnert M. D., Heckman T. M., 1995, ApJS, 97, 89
Levy R. C. et al., 2019, ApJ, 882, 84
Li J.-T., Wang Q. D., 2013a, MNRAS, 428, 2085
Li J.-T., Wang Q. D., 2013b, MNRAS, 435, 3071
Li J.-T., Li Z. Y., Wang Q. D., Irwin J. A., Rossa J., 2008, MNRAS, 390, 59
Li J.-T., Wang Q. D., Crain R. A., 2014, MNRAS, 440, 859

Li J.-T. et al., 2016, MNRAS, 456, 1723
Li J.-T., Bregman J. N., Wang Q. D., Crain R. A., Anderson M. E., Zhang S., 2017, ApJS, 233, 20
Li J.-T., Bregman J. N., Wang Q. D., Crain R. A., Anderson M. E., 2018, ApJ, 855, 24
Li J.-T., Hodges-Kluck E., Stein Y., Bregman J. N., Irwin J. A., Dettmar R.-J., 2019, ApJ, 873, 27
Li J.-T. et al., 2022, MNRAS, 515, 2483
Madau P., Haardt F., 2015, ApJ, 813, 8
Moshir M. et al., 1990, BAAS, 22, 1325
Murphy E. J. et al., 2011, ApJ, 737, 67
Putman M. E., Peek J. E. G., Joung M. R., 2012, ARA&A, 50, 491
Rand R. J., 1996, ApJ, 462, 712
Rand R. J., 1997, ApJ, 474, 129
Rand R. J., Kulkarni S. R., Hester J. J., 1990, ApJ, 352, L1
Reach W. T., Fadda D., Rand R. J., Stacey G. J., 2020, ApJ, 902, 28
Reynolds R. J., 1984, ApJ, 282, 191
Reynolds R. J., 1985, ApJ, 298, L27
Richards E. E. et al., 2018, MNRAS, 476, 5127
Rossa J., Dettmar R.-J., 2000, A&A, 359, 433
Rossa J., Dettmar R.-J., 2003, A&A, 406, 493
Rozas M., Beckman J. E., Knapen J. H., 1996, A&A, 307, 735
Rupke D. S. N. et al., 2019, Nature, 574, 643
Sanders D. B., Mirabel I. F., 1996, ARA&A, 34, 749
Sanders D. B., Mazzarella J. M., Kim D.-C., Surace J. A., 2003, AJ, 126, 1607
Sciama D. W., 1990, ApJ, 364, 549
Slavin J. D., Shull J. M., Begelman M. C., 1993, ApJ, 407, 83
Spector O., Finkelman I., Brosch N., 2012, MNRAS, 419, 2156
Strickland D. K., Heckman T. M., Colbert E. J. M., Hoopes C. G., Weaver K. A., 2004, ApJS, 151, 193
Sutherland R. S., Dopita M. A., 1993, ApJS, 88, 253
Tacchella S. et al., 2021, MNRAS, 513, 2904
Tody D., 1986, Proc. SPIE, 627, 733
Tüllmann R., Breitschwerdt D., Rossa J., Pietsch W., Dettmar R-J., 2006a, A&A, 457, 779
Tüllmann R., Pietsch W., Rossa J., Breitschwerdt D., Dettmar R-J., 2006b, A&A, 448, 43
Tully B., 1988, Nearby Galaxies Catalog. Cambridge Univ. Press, Cambridge
Vargas C. J. et al., 2018, ApJ, 853, 128
Vargas C. J., Walterbos R. A. M., Rand R. J., Still J., Krause M., Li J-T., Irwin J., Dettmar R-J., 2019, ApJ, 881, 26
Wang Q. D., Li J.-T., Jiang X.-C., Fang T., 2016, MNRAS, 457, 1385
Wiegert T., Irwin J., Arpad M. et al., 2015, ApJ, 150, 81
Wood K., Mathis J. S., 2004, MNRAS, 353, 1126
Wood K., Reynolds R. J., 1999, ApJ, 525, 799
Yoshida M. et al., 2002, ApJ, 567, 118
Zheng Y. et al., 2022a, MNRAS, 513, 1329
Zheng Y. et al., 2022b, Research in Astronomy and Astrophysics, 22, 085004
Zurita A., Rozas M., Beckman J. E., 2000, A&A, 363, 9
Zurita A., Beckman J. E., Rozas M., Ryder S., 2002, A&A, 386, 801

SUPPORTING INFORMATION

Supplementary data are available at *MNRAS* online.

appendix.tar.gz

Please note: Oxford University Press is not responsible for the content or functionality of any supporting materials supplied by the authors. Any queries (other than missing material) should be directed to the corresponding author for the article.

[1]*Department of Astronomy, Xiamen University, 422 Siming South Road, Xiamen, Fujian, People's Republic of China*
[2]*Purple Mountain Observatory, Chinese Academy of Sciences, 10 Yuanhua Road, Nanjing 210023, People's Republic of China*
[3]*Department of Astronomy, University of Michigan, 311 West Hall, 1085 S. University Ave, Ann Arbor, MI, 48109-1107, USA*
[4]*Department of Astronomy and Steward Observatory, University of Arizona, 933 N. Cherry Avenue, Tucson, AZ 85721, USA*
[5]*Max-Planck-Institut für Radioastronomie, Auf dem Hügel 69, 53121 Bonn, Germany*
[6]*Ruhr University Bochum, Faculty of Physics and Astronomy, Astronomical Institute, D-44780 Bochum, Germany*
[7]*Department of Physics and Astronomy, University of Manitoba, Winnipeg, Manitoba R3T 2N2, Canada*
[8]*CSIRO, Space and Astronomy, PO Box 1130, Bentley, WA 6102, Australia*
[9]*Department of Astronomy, Columbia University, New York, NY 10027, USA*
[10]*Department of Astronomy & Astrophysics, The University of Chicago, Chicago, IL 60637, USA*
[11]*Department of Physics and Astronomy, University of New Mexico, 210 Yale Blvd NE, Albuquerque, NM 87106, USA*
[12]*Department of Astronomy, University of Massachusetts, Amherst, MA 01003, USA*
[13]*Kavli Institute for Astronomy and Astrophysics, Peking University, Beijing 100871, People's Republic of China*
[14]*Instituto de Astrofísica de Andalucía (IAA-CSIC), Glorieta de la Astronomía, 18008, Granada, Spain*
[15]*Research Center for Intelligent Computing Platforms, Zhejiang Laboratory, Hangzhou 311100, People's Republic of China*

This paper has been typeset from a TEX/LATEX file prepared by the author.